IEEE Access
Multidisciplinary | Rapid Review | Open Access Journal

Received March 24, 2017, accepted May 25, 2017, date of publication May 31, 2017, date of current version June 28, 2017.

Digital Object Identifier 10.1109/ACCESS.2017.2710305

Single Image Dehazing via Large Sky Region Segmentation and Multiscale Opening Dark Channel Model

YUN LIU, (Student Member, IEEE), HEJIAN LI, AND MINGHUI WANG
College of Computer Science, Sichuan University, Chengdu 610065, China

Corresponding author: Minghui Wang (wangminghui@scu.edu.cn)

This work was supported in part by the National Natural Science Foundation of China under Grant 61071162 and in part by the Chengdu Science and Technology Project under Grant 2015-HM02-00080-SF.

ABSTRACT Outdoor images acquired under poor weather conditions are usually contaminated by suspended particles and aerosols in the atmosphere. These captured images easily suffer from contrast reduction, low visibility, and color distortion. In this paper, we develop a novel single image dehazing method based on large sky region segmentation and multiscale opening dark channel model (MODCM). First, a simple but effective method for large sky region detection based on SVM classification is presented, which can be considered as the first step of atmospheric light estimation. Then, two different strategies are utilized for obtaining a more accurate estimate of the atmospheric light according to the mentioned detection result. Furthermore, MODCM can adaptively make use of different patch sizes to calculate the dark channel according to different edge levels, which can prevent halo artifacts near edges of depth discontinuity. In addition, the gradient domain guided filter is adopted to refine the initial transmission map due to its accuracy near edges. Finally, the haze-free image can be obtained through correcting the colors of the sky region and combining the sky and non-sky region. Experimental results on different kinds of hazy images indicate that our proposed approach can produce the visually desirable results with genuine color and high scene visibility, even superior than the other state-of-the-art dehazing methods.

INDEX TERMS Dehazing, large sky region detection, atmospheric light, multiscale opening dark channel model(MODCM), gradient domain guided filter.

I. INTRODUCTION

With the development of modern science and technology as well as cost reduction, the computer vision systems have been widely applied for numerous applications such as outdoor monitoring, remote sensing, navigation, and intelligent vehicles. However, these computer vision systems are built on the basis of images with high visibility captured by digital camera. In the case of inclement weather especially on a foggy or hazy day, the light is scattered and attenuated by many suspended particles on its way from the object to the camera. Additionally, the light received by the digital camera is usually mixed into airlight reflected by the atmosphere. Thus, the captured image will be severely degraded by the presence of haze in the atmosphere. Therefore, restoring the haze-free images rapidly and efficiently is necessary for computer vision systems.

Generally speaking, image dehazing methods can be broadly categorized into two types, enhancement-based algorithms and physics-based algorithms. Enhancement-based algorithms, such as histogram-based dehazing method [1], wavelet fusion [2] and retinex [3], have been widely applied in image processing. Image enhancement based dehazing methods remove the haze aiming at compensating contrast and color of the degraded image but sacrifice the scene depth information. Furthermore, such methods fail to consider the formation principle of the hazy image and image degradation mechanism. Physics-based dehazing algorithms analyze the degradation process, build the atmospheric scattering model and inverse the degradation process to obtain the haze-free image. Nevertheless, the atmospheric scattering model is an ill-conditioned system of three equations and at least four unknown parameters for each pixel, which cannot be handled directly. To circumvent this problem, in earlier studies, several dehazing methods based on multiple images or additional information have been put forward. Multiple images based haze removal methods usually exploit

different degrees of polarization [4], [5] or the same scene taken under different weather conditions [6] to restore the haze-free image. Alternatively, three-dimensional (3D) models [7] or user inputs [8] are used to estimate the scene depth information for haze removal. Although the above methods can produce impressive dehazing results, they are not suitable for dynamic scenes dehazing and limited in real-life applications.

Accordingly, another class of dehazing methods only using a single input hazy image has attracted widespread attention due to the application restrictions of the aforementioned method, which relies on some prior knowledge or assumptions to remove the haze. For instance, Tan [9] removes the haze by focusing on maximizing the local contrast of the restored image, which mainly depends on two basic observations: one is that the haze-free image has much higher contrast than that of degraded image, and another is that the variation of airlight is solely associated with the distance from the scene to the observer and varies smoothly. However, the results of this method often suffer from oversaturated. Fattal [10] estimates the transmission map and then restores the scene radiance by using independent component analysis (ICA) under the assumption that the transmission and the surface shading are locally statistically independent. Nevertheless, this approach may be invalid in the condition of dense haze. Instead of trying to estimate the transmission map, Tarel and Hautire [11] take advantage of median filter to calculate the atmospheric veil from minimum color component. This method can perform very fast, but the median filter cannot preserve edge well and the desirable results cannot be achieved in some edges of depth discontinuity. On the basis of [11], Tarel *et al*. [12] extend previous dehazing algorithm for better dealing with road scenes under heterogeneous haze. He *et al*. [13] propose a novel prior-dark channel prior (DCP) for haze removal based on the statistical observation of outdoor haze-free images that most local non-sky patches in haze-free image possess some low intensity pixels at least one color channel. The outstanding dehazing results can be obtained by this method in most cases. Unfortunately, it cannot deal with some situations where the pixel intensity of local patch is similar to the atmospheric light such as the sky region. Subsequently, a series of works based on DCP are proposed to improve the drawbacks of the DCP method. In order to promote the computational efficiency, the guided filter is presented by He *et al*. [14] and adopted to refine the transmission map. Gibson *et al*. [15] make use of median filter instead of soft matting to reduce the time consumption. On the other hand, in terms of dehazing effect, Nishino *et al*. [16] model the hazy image formation using a factorial Markov random field (MRF) to obtain a more elaborate estimation for structural information of the scene. Wang *et al*. [17] estimate the transmission map in sky and non-sky region respectively, then combine them with a refine step, and restore the scene radiance finally. Meng *et al*. [18] restore the haze-free image by combining the inherent boundary constraint on the transmission map with a weighted L_1-norm based contextual regularization. Even though these improved approaches have achieved remarkable progress, there are still some shortcomings and need to be further studied. More recently, several researchers derive some multiple scattering models instead of the widespread dichromatic scattering model and apply it into single image dehazing. Li *et al*. [19] take multiple scattering effects into account and consider multiple scattering as a process of iterative smoothing. Meanwhile, some novel priors are proposed for haze removal. Zhu *et al*. [20] propose a novel prior knowledge for haze removal, namely color attenuation prior. Based on this prior, the scene depth of the hazy image is modeled as a linear model in which unknown parameters can be estimated with a supervised learning method. Choi *et al*. [21] put forward a referenceless perceptual fog density prediction model and exploit it to dehaze by multi-scale fusion. Cai *et al*. [22] adopt convolutional neural network (CNN) technique to develop an end-to-end system for haze removal. Among these methods mentioned above, DCP-based dehazing method provided by He *et al*. [13] is the most popular and cited so far.

For overcoming the left issues in the DCP-based methods, in this paper, we present a novel single image dehazing algorithm based on large sky region segmentation and multiscale opening dark channel model (MODCM). The key idea of our approach is to extract the large sky region from a single input hazy image, which is mainly based on two observations: first, the DCP-based haze removal methods tend to noise amplification and color distortion in the large sky region; second, the atmospheric light is primarily constrained in the sky region. The major contributions of this paper are outlined as follows:

- A simple yet effective method for large sky region detection is presented from the point of view of statistic. Through statistical analysis on massive hazy images with large sky region, we summarize three simple and intuitive features of large sky region in the hazy image and then train a two-class classifier to determine whether a pixel belongs to the sky region or not.
- Based on the mentioned detection result, two different strategies can be automatically selected to estimate the atmospheric light. Compared with previous methods, the proposed algorithm not only choose an appropriate strategy to estimate the atmospheric light according to whether the input image contains the sky region or not, but also be free of white objects or stochastic white noises.
- An improved dark channel model, called MODCM, is proposed for obtaining fine details of scene structure as well as preventing halo artifacts near depth edges. Meanwhile, the gradient domain guided filter [23] is applied to refine the coarse transmission map instead of soft matting or guided filter due to its accuracy near edges. To the best of our knowledge, this filter is introduced into dehazing application for the first time.

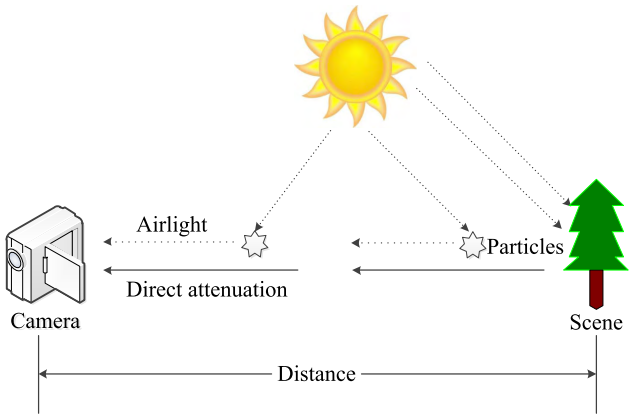

FIGURE 1. Hazy image formation based on atmospheric scattering model.

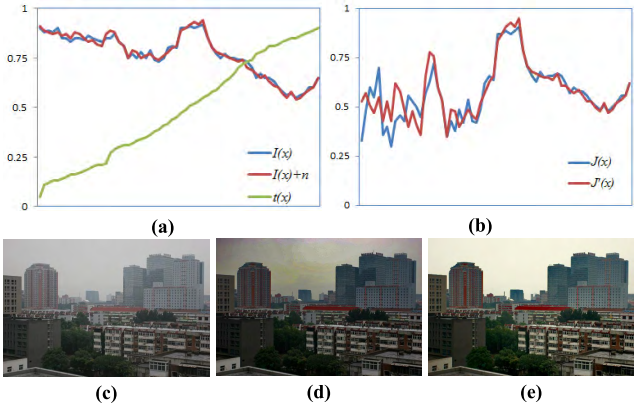

FIGURE 2. Noise amplification and color distortion. (a) 1D synthetic signals $I(x)$, $I(x)+n$ and $t(x)$; (b) the finally restored signals $J(x)$ and $J'(x)$; (c) The real hazy image; (d) Dehazed image by He *et al.* [13]; (e) Dehazed image by our approach. In (*a*) and (*b*), the *x-axis* and the *y-axis* represent the position and the intensity, respectively.

The remaining of this paper is organized as follows. Section II describes the formation process of a hazy image in brief and introduces the corresponding degradation model. The details of our proposed dehazing method are given in Section III. In Section IV, a series of experiments and analysis are conducted. Finally, Section V concludes our proposed haze removal method and future work are discussed at the same time.

II. BACKGROUND

On a hazy or foggy day, only a part of the scene reflected light can arrive the imaging equipment due to atmosphere absorption and scattering influenced by suspended particles, which makes the acquired image appear low overall contrast and faded colors. To describe and model this phenomenon, McCartney [24] proposed the atmospheric scattering model in 1976. Later, Narasimhan and Nayar [6] derive this model further, which is widely used computer vision and computer graphics now. Mathematically, the atmospheric scattering model can be described as:

$$I(x) = J(x)t(x) + A(1 - t(x)) \tag{1}$$

where x is the spatial coordinates of each pixel, $I(x)$ is the observed hazy image, $J(x)$ is the true scene radiance or hazy-free image, A is the global atmospheric light, which is generally assumed as a constant in each color channel, and $t(x)$ is the medium transmission, representing the portion of the light that arrives the camera. From Equation (1), the first part $J(x)t(x)$ is the direct attenuation term, representing how much the scene reflected light reaches the camera without scattering in the medium. The second component $A(1-t(x))$ is the airlight term, indicating the scattering light caused by the environmental illumination that scattered into light flux received by the camera. The goal of dehazing is to estimate $t(x)$ and A for acquiring the haze-free image $J(x)$ using Equation (1). Fig. 1 briefly shows the formation of a hazy image, which mainly consists of two parts: the attenuation and airlight mechanism.

Referring to the atmospheric scattering model, the transmission is relevant to the distance from the objects to the camera, which can be expressed as:

$$t(x) = e^{-\beta d(x)} \tag{2}$$

where β is the atmospheric attenuation coefficient, $d(x)$ represents the scene depth from the scene to the camera at the pixel x. β generally changes with the wavelength, but this constraint has been regarded negligible for reducing the number of unknown parameters in previous methods. Following this assumption, β can be considered as a constant in this paper. In Equation (2), it can be found that the transmission decreases as the scene depth increases, and vice versa. Assuming that the pixel x_∞ in the input image is infinitely far apart from the camera, the corresponding transmission $t(x_\infty)$ is close to 0. Substitute it into Equation (1), and we have:

$$I(x_\infty) = J(x_\infty)t(x_\infty) + A(1 - t(x_\infty)) \to A \tag{3}$$

As pointed in Equation (3), the intensity of the furthest pixel x_∞ in $I(x)$ can be approximately served as the value of the atmospheric light. As is well known, the distance between the sky region and the camera tends to infinity compared with other scenes in $I(x)$. If a hazy image $I(x)$ contains sky region, the value of the atmospheric light should be primarily restricted in the sky region. Therefore, extracting the sky region of the input hazy image can be regarded as the first step of atmospheric light estimation.

III. OUR DEHAZING METHOD

It should be noted that the DCP rule can still hold for a small sky region within the hazy image because of the effect of the neighborhood pixels around the sky region. However, when an input hazy image contains a large sky region, the conventional DCP-based dehazing methods may be invalid. Moreover, these methods may magnify noise and cause color distortion and shift in the large sky region. This is one of the most important reasons that we detect whether the hazy image contains a large sky region or not. Fig. 2(a) and 2(b) indicate that when 1D synthetic signals

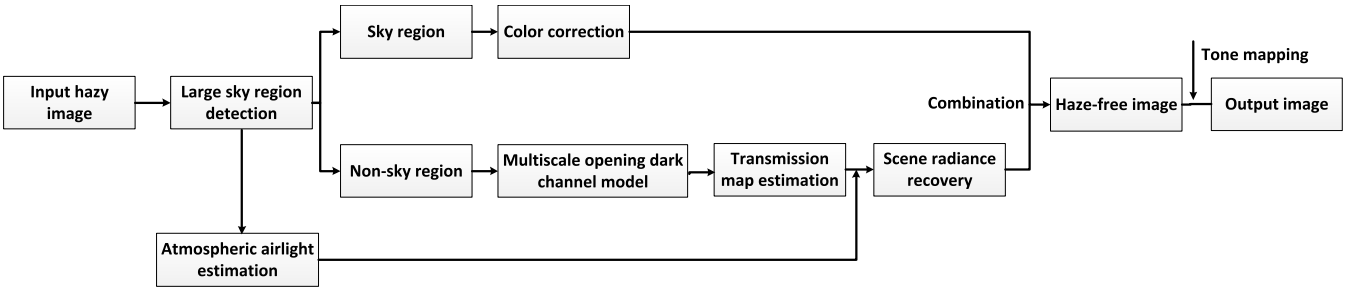

FIGURE 3. Flowchart of the proposed dehazing method.

$I(x)$ and $I(x) + n$ have a very small difference because of the noise, the finally restored two signals $J(x)$ and $J'(x)$ are very different for the part with small transmission $t(x)$. Fig. 2(c)-2(e) show that the dehazed image by the conventional DCP-based method may produce serious noise and color distortion, while our dehazing approach can preserve the authenticity of the colors.

On the basis of the mentioned analysis, we propose a novel and plausible dehazing method based on large sky region segmentation and MODCM. The basic idea of our method is to extract the large sky region from an input hazy image, and the non-sky and sky region are handled with different treatment. Fig. 3 provides the flowchart of the proposed dehazing method, which is mainly composed of five parts: large sky region detection, atmospheric light estimation, multiscale opening dark channel model, transmission map estimation and scene radiance recovery.

A. LARGE SKY REGION DETECTION

In general, sky region detection is a challenging problem due to its diversity and similarity. To the best of our knowledge, most existing detection methods are mainly based on color prior, histogram analysis and threshold methods. Although these methods can produce a good effect in some certain situations, they may not be applied well to sky region detection in the hazy image and some related parameters of detection algorithms are needed to be set by user input. When it comes to sky region detection of the hazy images, the white objects are easily mistaken for sky region and the clouds may be classified as non-sky region. Moreover, when the hazy image contains a very small sky region, it is hardly to detect the sky region accurately and the DCP rule remains valid under this circumstance. Therefore, different from other sky region detection approaches, the proposed method focuses on large sky region detection in the hazy images and considers this task as a two-class classification problem. In order to distinguish the sky region from the input hazy image better, we first investigate some intuitive and effective features of the sky region based on statistical observation and then train a pixel-wise classifier to detect sky regions by a supervised learning method.

To prepare the dataset for statistical analysis and training classification model, we collect more than 300 hazy images

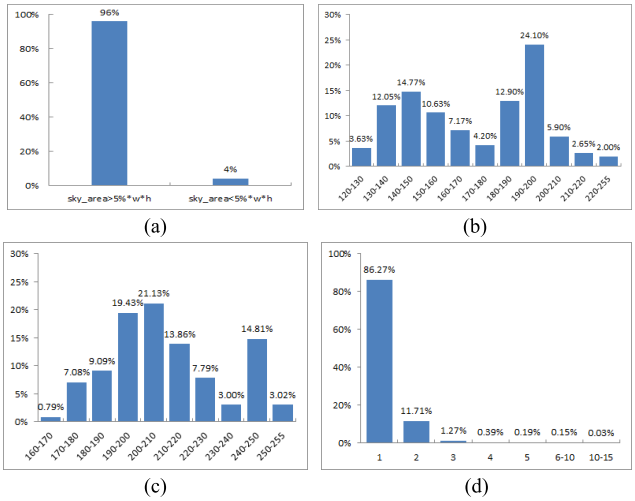

FIGURE 4. Statistical results of three features of large sky region. (a) Area of the sky region. (*x-axis*:the area of sky region, *y-axis*:the proportion) (b)-(c) Intensity distribution of the pixel-based dark channel and bright channel. (*x-axis*: the intensity, *y-axis*:the proportion) (d) Gradient histogram distribution. (*x-axis*:the gradient value, *y-axis*:the proportion).

containing sky region from Google Images, Flickr, and Internet to form a dataset. Then, about 100 images of them are randomly selected as the statistical dataset. Because the features of the sky region is the focus of our attention, we manually try to cut out the sky region of the selected images to conduct statistical analysis on them, three simple and intuitive features are summarized as follows:

- Area. The large sky region generally has greater area than 5% of the whole image. Fig. 4(a) shows 96% hazy images conform to the above feature, while only 4% of test images have less than 5% of the whole image. Therefore, this feature can be used to eliminate mistaken sky regions, which can be considered as a post-processing step.
- Brightness. It is generally known that the sky region has higher brightness than other scenes in hazy image. To differentiate this feature better, the pixel-based dark channel and bright channel prior are utilized to measure whether a pixel belongs to sky region or not. In the pixel-based dark channel, the non-sky region will be darker, while the sky region almost remains the original brightness intensity. Similarly, for the pixel-based

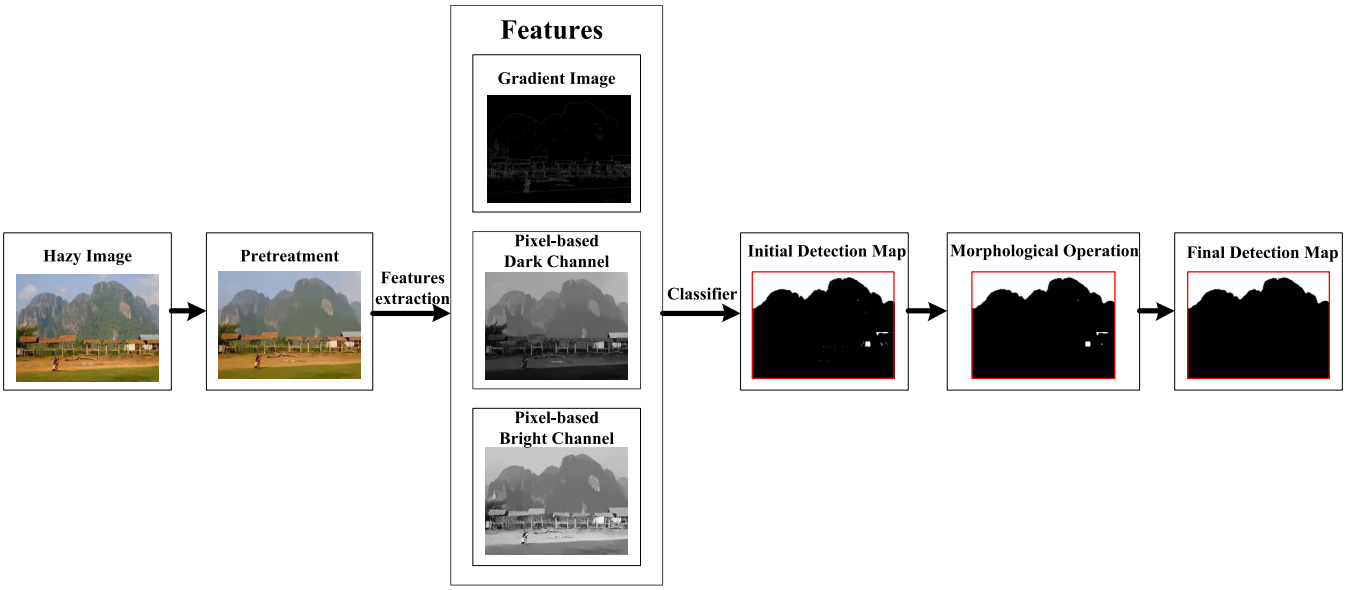

FIGURE 5. Flowchart of large sky region detection.

bright channel, the brightness feature of the sky region will be more highlighted to be extracted easily. Fig 4(b) and 4(c) show the intensity distribution of the sky region, in which the brightness of the pixel-based dark channel and bright channel is mainly concentrated in the range of [120,220] and [170,255].

- Gradient. The gradient varies slowly in the sky region. As pointed in Fig. 4(d), the gradient histogram of sky region of hazy images is in the range of [1,15], in which the gradient magnitude between 0 and 5 accounts for the largest proportion. Moreover, through exploring the gradient histogram distribution of a large number of hazy images, we find that the gradient of the sky region is close to the gradient values of the highest frequency group of the gradient histogram, as shown in the third columns of Fig. 6.

Next, to construct a classifier model, the training dataset including about 200 hazy images is chosen from the assembled dataset above. It is worth noting that the pixel is the basic label unit in our method. Therefore, pixels of the sky region are labeled the positive samples, while those of the non-sky region are defined as the negative samples. Based on the mentioned statistical characteristics (i.e. gradient prior, pixel-based dark channel and bright channel prior), we train a two-class classifier to identify whether a pixel belongs to the sky regions in a pixel-wise manner. In machine learning methods, the support vector machine (SVM) method is adopted to train the classification model, which is a supervised learning method. Furthermore, we also use morphological operators to refine some wrong detection results. Here are the detailed steps of our proposed detection algorithm. Fig. 5 shows an example of sky region detection to understand the each stage of method clearly.

Step 1. First, the input hazy image is preprocessed through an effective image smoothing method [25] for sharpening strong edges while eliminating low-amplitude scene structure. This pretreatment method can smooth weak edges such as clouds in sky region and highlight strong edges.

Step 2. After pretreatment, three features (i.e. gradient, pixel-based dark channel and bright channel) of each pixel are extracted for detecting whether a pixel is a part of sky regions by using a trained two-class SVM classifier. We regard this classification results as the initial detection map I_{bin}.

Step 3. To optimize the connected region of the initial detection map, morphological opening and closing operations are utilized for refining the classification results I_{bin} consecutively.

Step 4. Finally, retain the white region whose area should be greater or equal to 5% of the whole image according to the "Area" feature above. This constraint can effectively reduce possible misclassification. The white region in the final detection map represents the large sky region of the hazy image, while the black region stands for the non-sky region.

Figure 6 provides our detection results using the proposed algorithm, which are almost same as human visual effects. When the hazy images contain no sky region or a tiny sky region, the detection resultant images are totally black.

B. ATMOSPHERIC LIGHT ESTIMATION

The atmospheric light plays an important role for restoring the hazy image, which influences the global illumination and colors of haze-free images. Inaccurate estimation of the atmospheric light may lead to poor dehazing performance. In this section, some typical estimation methods for the atmospheric light will be discussed and an adaptive and robust estimation method is presented according to the mentioned

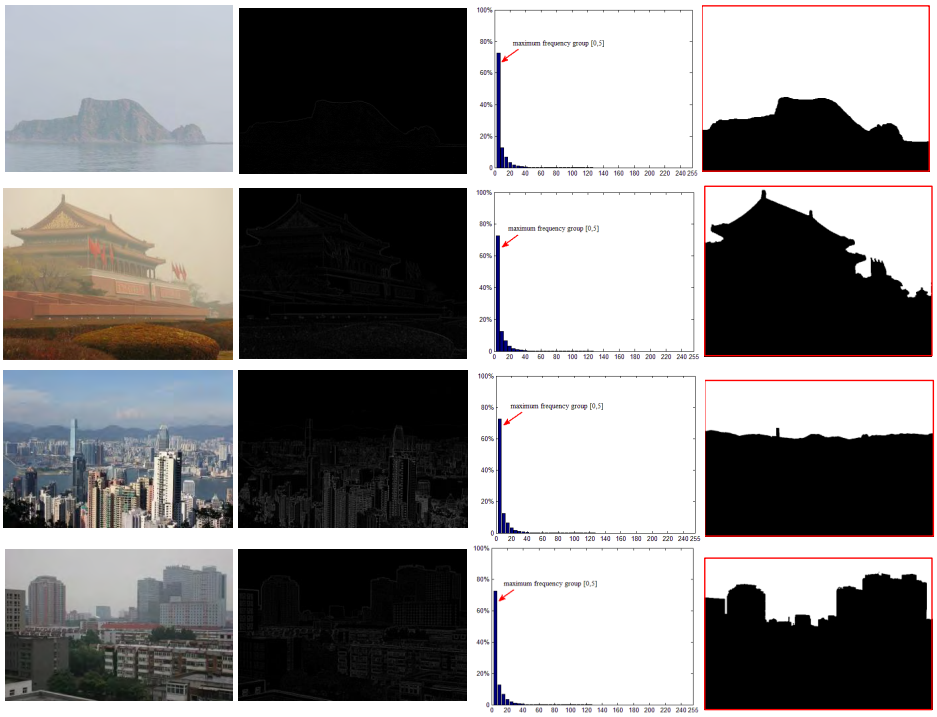

FIGURE 6. Results of large sky region detection. The first, second, third and fourth columns stand for the input hazy images, gradient images, gradient distributions and final detection results, respectively.

detection result. Tan [9] assumes that the brightest pixel in the input image is saturated with dense haze and treats it as the estimation value of the atmospheric light. However, this method can be easily influenced by the white objects, which causes over estimation of the atmospheric light. He *et al*. [13] estimate the atmospheric light by picking the top 0.1 percent brightest pixels in the dark channel of the hazy image and select the highest intensity pixel of them in the input hazy image as the atmospheric light. Nevertheless, He *et al*.'s method may produce a wrong estimation value because of the effect of white objects or artificial light in the input image. Kim *et al*. [26] present a fast estimation algorithm based on the quad-tree subdivision. Since Kim's approach choose the pixel position of the minimum distance from pure white vector (255,255,255) as the atmospheric light value in the final selected block, results of this method exhibit sensitivity to the white noise. Yu *et al*. [27] decompose the input image into sky region and non-sky region, and then select the brightest pixel as the atmospheric light in the sky. Unfortunately, this method is not suitable for the image containing no sky region. Furthermore, this method may be also sensitive to the white noise similar to Kim *et al*.'s method [26]. In summary, there are two major problems in existing estimation methods. First, the estimation value of atmospheric light can easily be affected by the white objects. Second, these methods are sensitive to the random white noise.

To overcome these limitations, inspired by Kim [26], we present a robust estimate method based on the quad-tree division and our detection result of large sky region, which can choose different strategies to calculate the atmospheric light. According to Equation (3), if the input hazy image includes sky region, the atmospheric light should be constrained in sky region, and conversely if not, an improved quad-tree division estimate method is used. Here are the detailed steps of our method.

Step 1. We first detect whether the input image contains a large sky region or not. If yes, continue to the Step 2. Otherwise, continue to Step 3.

Step 2. If the input hazy image contains a large sky region, the average intensity of the top 0.1 percent brightest pixels of the sky region is selected as the atmospheric light in each color channel, which can alleviate the effect of the white noise in the sky region. Then, the algorithm terminates.

Step 3. If the input hazy image contains no sky region, we divide it into four rectangle sub-blocks, and then compute the weight of each block. The calculation formula of the weight is given as below:

$$S_{B_i} = \frac{1}{3} \sum_{c \in \{r,g,b\}} \left| avg\left(I^c_{B_i}\right) - \sigma^c_{B_i} \right| \tag{4}$$

where B_i $(i = 1, 2, 3, 4)$ stands for each rectangle sub-block, $avg(I^c_{B_i})$ and $\sigma^c_{B_i}$ are the average intensity and standard deviation of sub-block in each color channel c, respectively.

Step 4. Retain the sub-block with the highest score. If the area of the selected sub-block is larger than the previously set threshold, this selected sub-block will go back to Step 3 and need to be divided into four parts further. Otherwise, continue

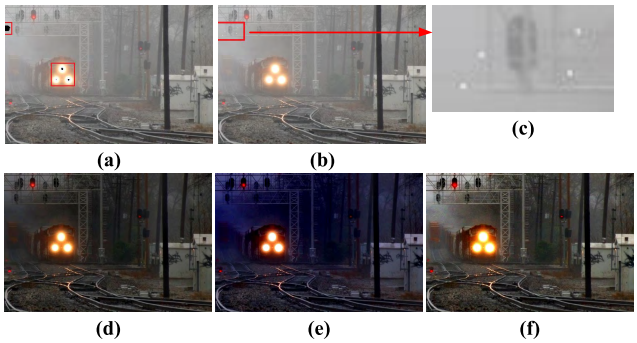

FIGURE 7. Comparison with other famous methods. (a) Candidate region of the atmospheric light estimated by He *et al*. [13]. (b) Candidate region obtained by Kim *et al*. [26] and ours. (c) Enlarged result indicated with red rectangle in (b). (d) Dehazed image using the atmospheric light estimated by Tan's method, He's method, and Kim's method. (e) Dehazed image by Meng's method. (f) Dehazed image by our method.

to Step 5. In our experiments, we set the threshold as $5\%*w*h$ empirically, where w and h represent width and height of the input image.

Step 5. To prevent the effect of the white noise, we use gray-scale erosion by calculating the dark channel of the final selected sub-block, marked as S_{dark}.

Step 6. Finally, we pick the top 10 percent brightest pixels in S_{dark}, and then consider the pixel of the minimum distance from the vector (255,255,255) as the atmospheric light.

Note that our proposed estimation method is different from any existing algorithms. In this section, our main contributions mainly consist of the following aspects: first, two different strategies are adopted to obtain a more accurate atmospheric light according to whether the input image contains large sky region or not; second, we make use of a series of post-processing to reduce the effect of white noises.

In order to verify how well the proposed estimation method performs, four famous and competing algorithms (i.e. Tan [9], He *et al*. [13], Meng *et al*. [18] and Kim *et al*. [26]) are selected for comparison. For fair comparison, we recover the scene radiance using He's method with different estimation approaches. It is worth noting that we should pay attention to the authenticity of the colors and the brightness in the dehazed image. Fig. 7 and Table 1 provide the comparison results and the estimate values of atmospheric light using five different methods, respectively. Owing to the brightest pixel in the input image, Tan's method always chooses the train light as the estimate value. Fig. 7(a) shows that the candidate region of the atmospheric light estimated by He's method also locates the train light, which causes an overestimation of the atmospheric light. Hence, the brightness of the restored haze-free image is rather dim due to an inaccurate estimation. Similarly, Meng's method is also affected by the train light. Moreover, we add stochastic white noises in the red rectangular block for verifying the robustness of our proposed estimation method, as indicated in

TABLE 1. Atmospheric light values estimated by five different methods.

Methods	Atmospheric light value
Tan's method [9]	(255,255,255)
He's method [13]	(255,255,255)
Meng's method [18]	(253,253,224)
Kim's method [26]	(255,255,255)
Ours	(192,192,193)

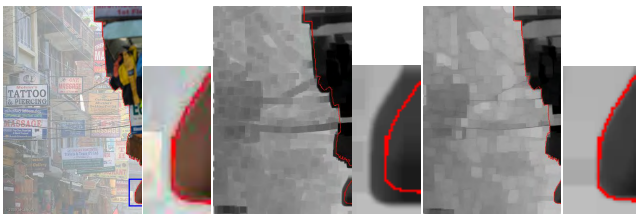

FIGURE 8. Comparison between the dark channel and the opening dark channel. (a) Input hazy image, the red line represents the edges with depth jumps. (c) Dark channel. (e) Opening dark channel. (b), (d) and (f) are the enlarged results indicated in the blue rectangle of (a), (c) and (e).

Fig. 7(b)-7(c). The candidate atmospheric region using Kim's method locates the red rectangle, however the stochastic white noise is considered as the estimate due to the minimum distance from pure white vector. Although the candidate region with our method is similar to Kim's, our approach can avoid the effect of stochastic white noises. From Fig. 7(d)-7(f), other estimate methods may exhibit low brightness or color shifts in the dehazed image, while our method can preserve the initial color and appropriate brightness due to using a more accurate atmospheric light.

C. MULTISCALE OPENING DARK CHANNEL MODEL (MODCM)

Through statistical analysis on massive outdoor haze-free images, He *et al.* [13] propose an observation that most local non-sky patches in outdoor haze-free images exist some pixels whose intensity are very low and close to zero in at least one color channel. Given a color image I, the mathematical expression of the dark channel I^{dark} is defined:

$$I^{dark}(x) = \min_{y\in\Omega(x)}\left(\min_{c\in\{r,g,b\}} I^c(y)\right) \tag{5}$$

where c stands for a color channel and $\Omega(x)$ represents a local patch centered at pixel x. In most cases, the excellent result can be yielded using this dark channel model. However, when the sliding local patch moves some edge regions of depth discontinuity, the dark region of the dark channel image may expand outward along edge direction, as shown in Fig. 8(c)-8(d). Under such circumstance, the restored haze-free image will generate obvious halo artifacts in edges with depth jumps. This is caused by the fact that the minimum filter is performed in the local patch and the pixel intensity over the entire local patch will be covered by the minimum pixel value. To suppress this effect, the morphological open

operator is used for replacing the minimum filter. Formally, the opening dark channel I^{odark} is achieved as follows:

$$I^{odark}(x) = \underset{y \in s(x)}{open}\left(\min_{c \in \{r,g,b\}} I^{c}(y)\right) \tag{6}$$

where $s(x)$ is structure element centered at pixel x. The morphological open operator can be considered as image erosion and dilation consecutively, which can effectively counteract the effect of edge expansion and keep edges unchanged. To intuitively compare the difference between the dark channel and opening dark channel, we use the red line to mark the edge region with large depth jumps by manually, as indicated in Fig. 8(a). Fig. 8(c) and 8(e) show the comparison result between the dark channel and opening dark channel. To observe the differences clearly, the results of the blue rectangle are also enlarged, as shown Fig. 8(b), 8(d) and 8(f). The dark channel easily suffers from edge coverage, while the edge regions of the opening dark channel almost remain unchanged.

In addition, there still exists an important issue about the selection of the patch size which is worthy of exploration and study. The patch size is a key parameter affecting the final dehazing performance. A larger patch size is more accordant with the DCP rule because of containing more dark pixels and the stronger halo artifacts are also produced in depth edges simultaneously. Conversely, a smaller patch size can reduce the halo artifacts effectively, but this will make the restored image oversaturated. Even for the opening dark channel, the size of structure element still needs to be set and the dehazing effect is also affected inevitably.

Motivated by multiscale strategy, a simple and intuitive solution is to fuse multiple opening dark channel images for jointing their merits of different patch sizes, called naive fusion method. The large patch size will not cause image over-enhancement and the small patch size can avoid halo artifacts near edges with depth jumps. The key to combine these two advantages is to construct the effective fusion decision map that can exhibit edge region with depth discontinuity. Since the opening dark channel can represent the depth variation information to a certain degree, canny operator is adopted to detect the edge of the opening dark channel and then image dilation is applied for neighborhood transition. The expression of the fused opening dark channel I^{fodark} can be formulated as:

$$I^{fodark}(x) = \begin{cases} \underset{y \in s_1(x)}{open}\left(\min_{c \in \{r,g,b\}} I^{c}(y)\right) & BDM(x) == 1 \\ \underset{y \in s_2(x)}{open}\left(\min_{c \in \{r,g,b\}} I^{c}(y)\right) & otherwise \end{cases} \tag{7}$$

where BDM is the binary decision map, determining which regions are used the small size s_1 or large size s_2. In terms of choosing the small patch s_1, we set the structure element size as $3 * 3$ for extract the scene structure details of depth discontinuity better. The large size s_2 is set $15 * 15$, which has proved in the literature [13].

Fig. 9 shows the comparison results between different sizes and naive fusion method. The restored haze-free image using the small patch size $3 * 3$ brings out the over-enhancement effects in the white window, as shown in the red rectangle of Fig. 9(f). For the large patch size $15 * 15$, serious halo artifacts appear near depth edges in Fig. 9(g). The naive fusion method completely avoids the drawbacks of the small size and reduce halo artifacts to some extent. Unfortunately, there still exist some halo artifacts in the neighborhood regions of depth edges. This is because of the non-edge regions still are affected by the edge pixel in some cases. As pointed in Fig. 9(h), even though the point A locates in the depth continuous regions, it still will be influenced by the edge pixel point B owing to using the large patch size $15 * 15$ determined by the fusion rule.

To tackle this issue, a superior approach using multiscale adaptive patch sizes according to different edge levels is put forward, called multiscale opening dark channel model (MODCM). The basic idea of our proposed method is to decompose depth variations into three levels by image dilation twice. More specifically, on the basis of the naive method, image dilation operation is performed on the BDM again and the gray value of the second expansion regions is marked as 0.5. Accordingly, the decision map of MODCM is reconstructed containing three colors: white, gray and black, respectively representing edge regions of depth discontinuity, neighboring regions of depth edges and depth continuity regions. Then, the selection of different patch sizes $size(x)$ can be formulated as:

$$size(x) = \begin{cases} s_1 & TDM(x) == 1 \\ min(max(s_1, \omega), s_2) & TDM(x) == 0.5 \\ s_2 & TDM(x) == 0 \end{cases} \tag{8}$$

where TDM is the three-color decision map. In the depth edges and non-edge regions, the patch sizes are set as s_1 and s_2. For the gray region, ω can be adaptively selected as the maximum size in the range of $[s_1,s_2]$ under the prerequisite that the local patch dose not include the depth edges regions (i.e. white regions). Then, the multiscale opening dark channel I^{modark} can be expressed as:

$$I^{modark}(x) = \underset{y \in size(x)}{open}\left(\min_{c \in \{r,g,b\}} \left(I^{c}(y)\right)\right) \tag{9}$$

In terms of the structuring size of image dilation, the dehazing performance tends to stable for most hazy images when the structuring size of the first and second dilation is set $5 * 5$ and $15 * 15$, respectively. In future, we will use [33] to search the optimal parameters for achieving the best dehazing result.

In Fig. 10, the input image is divided into three edge levels and different patch sizes are applied in different color regions. The restored haze-free image using multiscale opening dark channel can alleviate the halo artifacts further, such as the red rectangle of Fig. 10(d). In order to verify which algorithms perform better, the dark channel provided by He *et al.* [13] and other three methods (i.e. opening dark

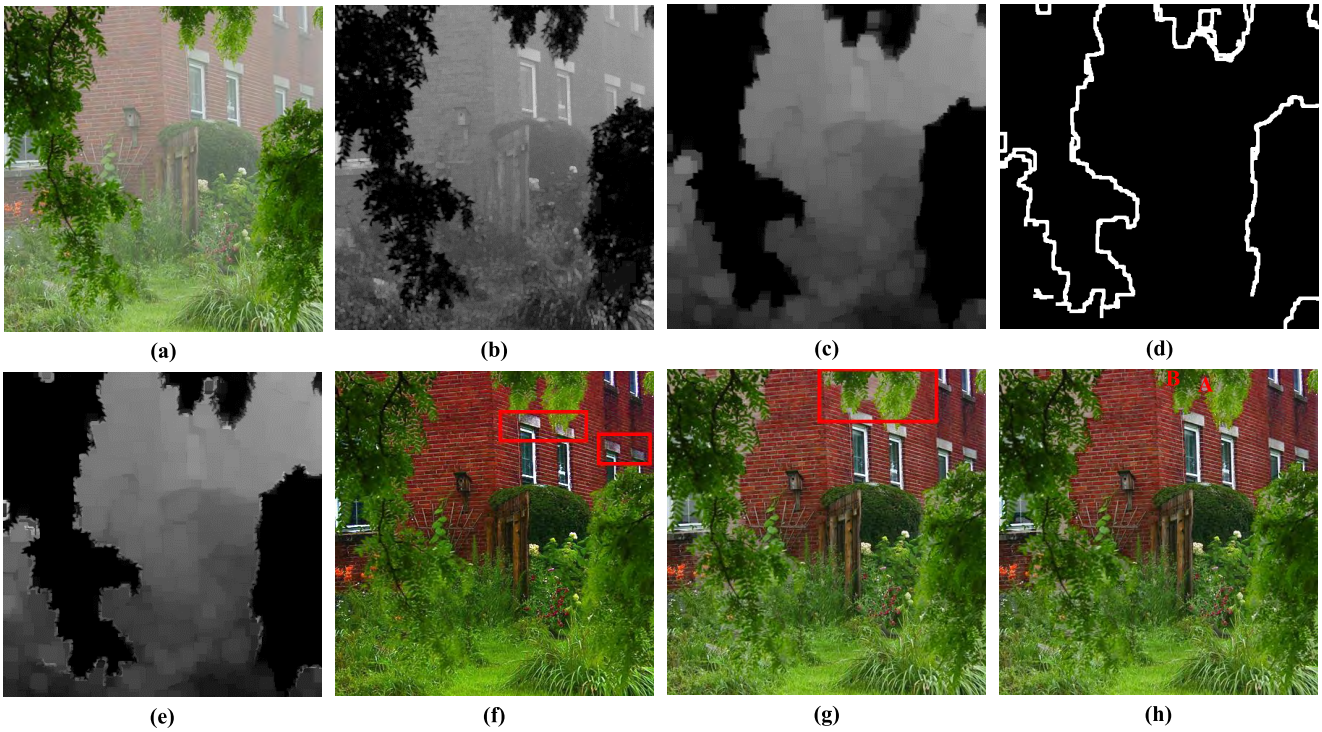

FIGURE 9. Fused opening dark channel obtained by naive fusion method. (a) Input hazy image. (b) Opening dark channel using the small size $3 * 3$. (c) Opening dark channel using the large size $15 * 15$. (d) Binary decision map (BDM). (e) Fused opening dark channel. (f)-(h) are the restored haze-free image using (b), (c) and (e), respectively.

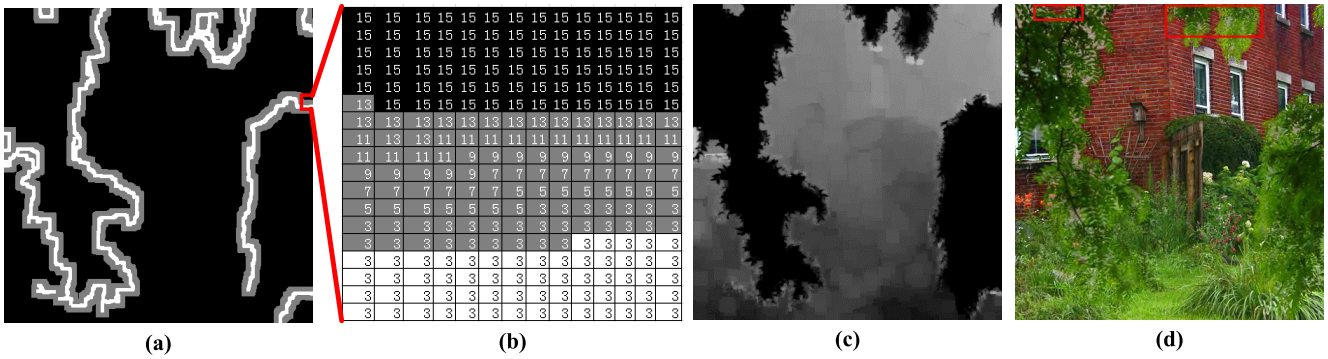

FIGURE 10. Multiscale opening dark channel. (a) Three-color decision map (TDM). (b) Adaptive patch sizes in the red rectangle of (a). (c) Multiscale opening dark channel. (d) Restored haze-free image using (c).

channel, fused dark channel , multiscale opening dark channel) are compared, as indicated in Fig. 11. It can be found in Fig. 11(j)-11(m) that the halo artifacts are reduced gradually. Therefore, the dehazing result by the proposed multiscale opening dark channel can avoid the halo artifacts near edges with depth discontinuity to a certain extent even without the refinement operation.

D. TRANSMISSION MAP ESTIMATION

According to the atmospheric scattering model and the proposed multiscale opening dark model, the initial transmission map $\tilde{t}(x)$ can be obtained:

$$\tilde{t}(x) = 1 - \frac{I^{modark}(x)}{\min\limits_{c\in\{r,g,b\}}(A^c)} \tag{10}$$

It is worth noting that there still exist block artifacts in the initial transmission map due to using block operation. Therefore, the initial transmission map should be refined further. As for the choice of the refinement algorithm, the computational complexity and effect should be concerned. Most researchers use guided filter [14] to refine the rough transmission map, which can reduce the calculation time greatly. However, the local linear model used in guided filter cannot stand for the image well near some edges, which can lead to halo artifacts. In addition, the guided filter cannot preserve edges well in some cases due to considering image filtering processing and edge-preserving process together. For solving the above problems, a gradient domain guided filter is proposed by Kou *et al*. [23], which has been applied in many fields, such as tone mapping of high dynamic

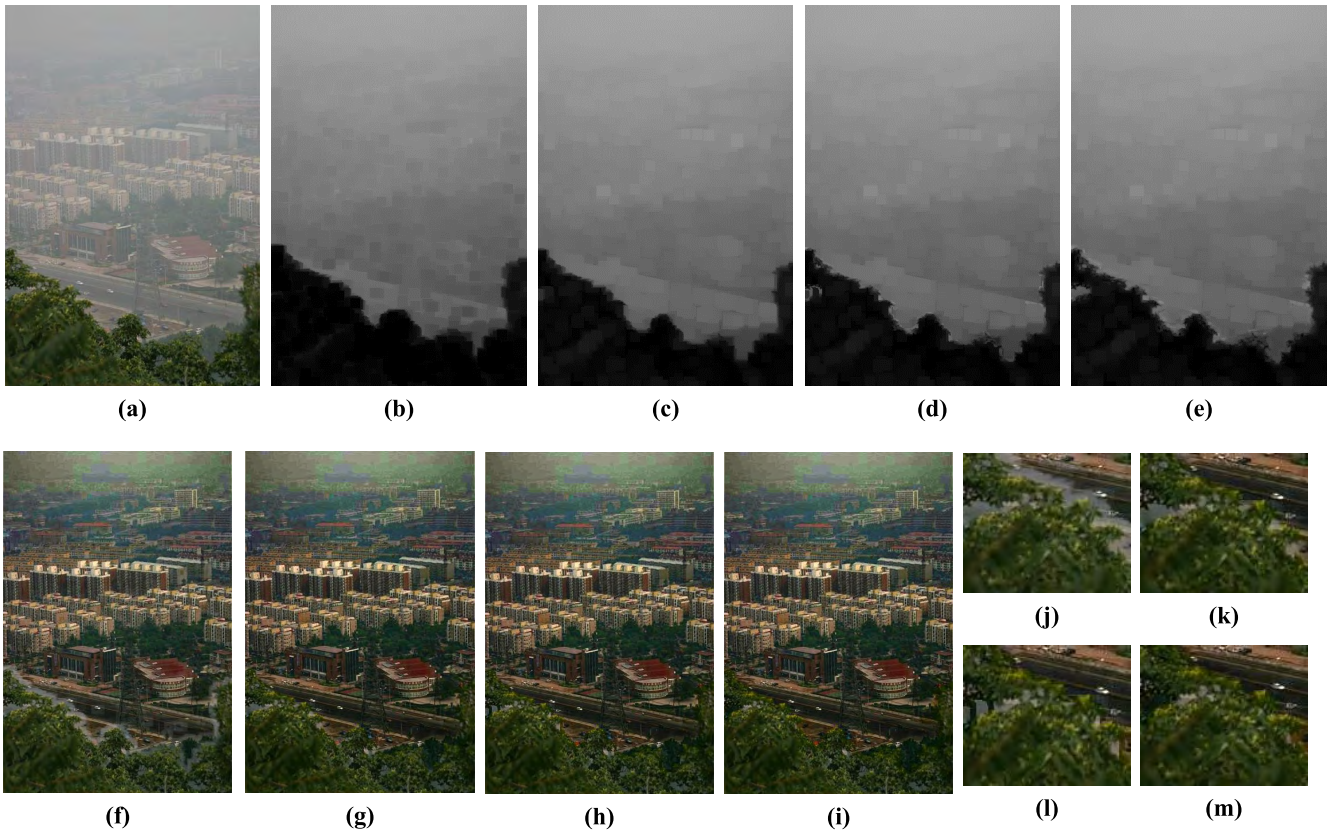

FIGURE 11. Comparison results of the dark channel and haze-free images without refinement obtained by four different methods. (a) Input hazy image. (b) Dark channel. (c) Opening dark channel. (d) Fused dark channel. (e) Multiscale opening dark channel. (f)-(i) are the restored haze-free image using (b)-(e). (j)-(m) are the enlarged results of local region of (f)-(i).

range (HDR) images, image saliency detection, etc. Contrast to the guided filter, the gradient domain guided filter incorporates an explicit first-order edge-aware constraint in the regularization terms, which is different from the guided filter. Because of this, edges are preserved much better using the gradient domain guided filter than the guided filter. In addition, the gradient domain guided filter has the same low computational complexity as the guided filter. On the basis of the mentioned analysis, the gradient domain guided filter is more appropriate for refining the coarse transmission map, which is the first time to apply it into dehazing application to the best of our knowledge.

E. SCENE RADIANCE RECOVERY

The sky region extracted from the hazy image generally does not contain texture details. However, it may appear yellowish because of the presence of haze. Therefore, color correction should be carried out in the sky region. There are many algorithms to correct the color of the image, such as grey world model, tone mapping, perfect reflector, etc. In our method, auto white balance is utilized to correct the colors of sky region, which is based on the statistical characteristics of images proposed by Weng *et al*. [28]. Moreover, this method exploits a dynamic threshold instead of the preset threshold without user inputs.

For the non-sky region, the atmospheric light A and the fine transmission map $t(x)$ can be obtained using the proposed method. Then, we substitute them into Equation (1) and rewrite it:

$$J^{non-sky}(x) = \frac{I(x) - A}{max\left(min\left(t(x), 0.1\right), 0.9\right)} + A \quad (11)$$

where $t(x)$ is constrained in the range of [0.1,0.9] for inhibiting too much noise. Then, by means of combining the sky region and non-sky region, the haze-free image $J(x)$ can be acquired. It is worth noting that if the input hazy image contains no sky region, the restored haze-free image can be obtained using Equation (11) directly. Finally, since the transmission map estimated under the DCP rule is smaller than the actual value, the brightness of the restored image will be darker than the real haze-free image. Therefore, a simple tone mapping method is used for make the restored image more realistic, which is provide by Drago *et al*. [29]. Given the restored haze-free image, the final output image J^{out} can be expressed as:

$$J^{out}(x) = \frac{J_{dmax} \cdot 0.01}{\lg\left(J^c_{max} + 1\right)} \cdot \frac{\ln\left(J^c(x) + 1\right)}{\ln\left(2 + \left(\left(\frac{J^c(x)}{J^c_{max}}\right)^{\frac{\ln(b)}{\ln(0.5)}}\right) \cdot 8\right)} \quad (12)$$

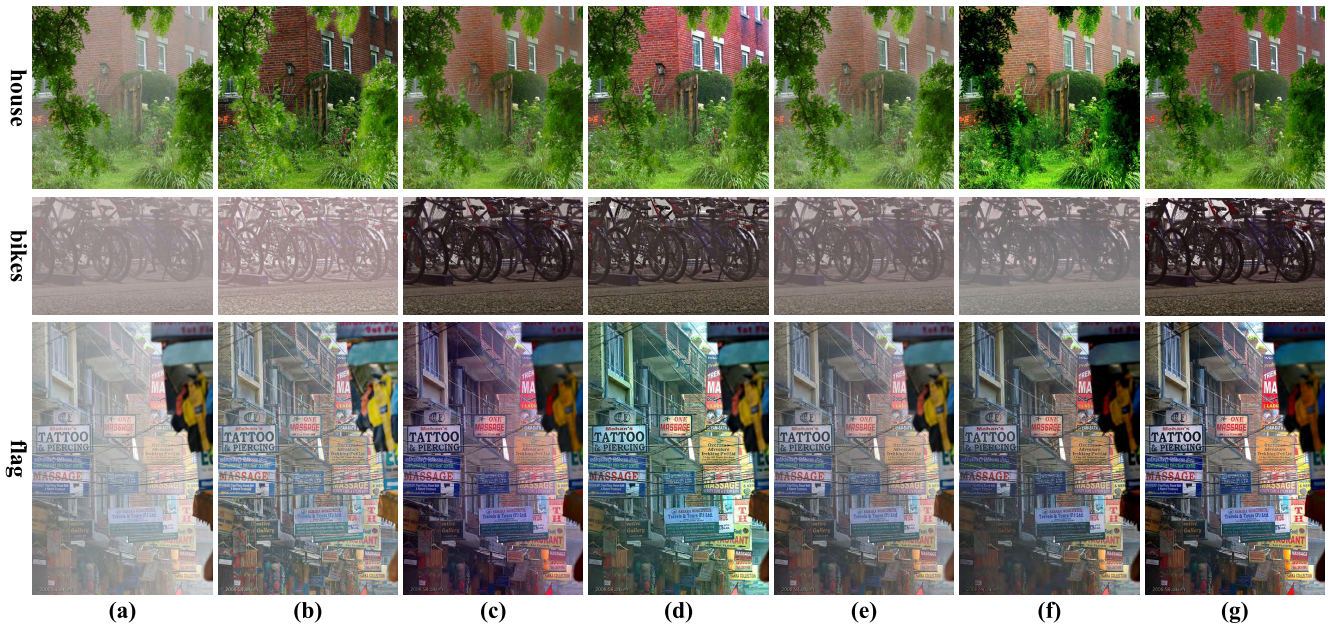

FIGURE 12. Comparison dehazing results on natural hazy images obtained by different approaches. (a) Input hazy image. (b) Tarel *et al.*'s results. (c) He *et al.*'s results. (d) Meng *et al.*'s results. (e) Zhu *et al.*'s results. (f) Choi *et al.*'s results. (g) Our results.

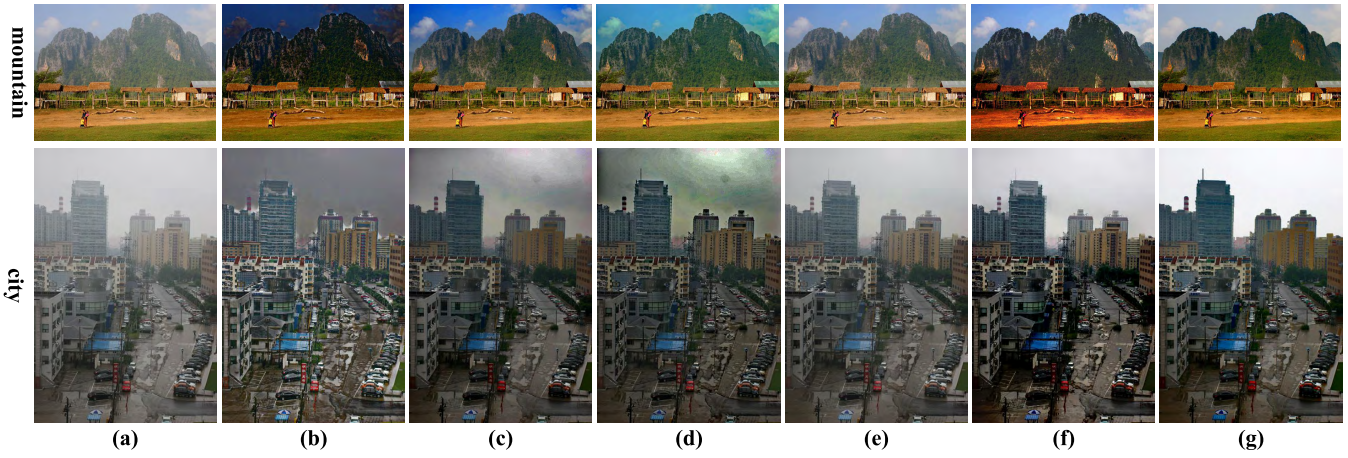

FIGURE 13. Comparison dehazing results on hazy images containing large sky region. (a) Input hazy image. (b)Tarel *et al.*'s results. (c) He *et al.*'s results. (d)Meng *et al.*'s results. (e) Zhu *et al.*'s results. (f) Choi *et al.*'s results. (g)Our results.

where J_{dmax} represent the maximum brightness intensity that the output can display, J^c_{max} is the maximum pixel intensity of J^c, and the bias parameter b is used for adjusting compression of high values and visibility of details in dark regions. The reference value of parameters J_{dmax} and b are set as 100 and 0.85 according to [29].

IV. EXPERIMENTAL RESULTS AND DISCUSSION

In order to demonstrate the effectiveness and robustness of the proposed dehazing approach, we conduct three groups of experiments on different kinds of hazy images, as pointed in Fig. 12-14. All experiments in this paper are implemented on a personal computer using MATLAB R2014a with a 2.2GHz Inter Pentium Dual Processor and 4 GB RAM. In terms of dehazing effect, we select some public hazy images for testing and choose five famous and competing methods (i.e. Tarel and Hautire [11], He *et al.* [13], Meng *et al.* [18], Zhu *et al.* [20], Choi *et al.* [21]) for comparison. For fair comparison, the parameters of five comparative algorithms are set to be optimal according to the respective publications. The code of Tarel *et al.*'s, Meng *et al.*'s, Zhu *et al.*'s and Choi *et al.*'s methods are available online for public use. In He *et al.*'s method, we use the guided filter [14] instead of soft matting [34] to refine the initial transmission map.

A. QUALITATIVE COMPARISON

Fig. 12 shows the dehazing results for natural hazy images using different methods. For the hazy image "house", serious halo artifacts are introduced into the restored images

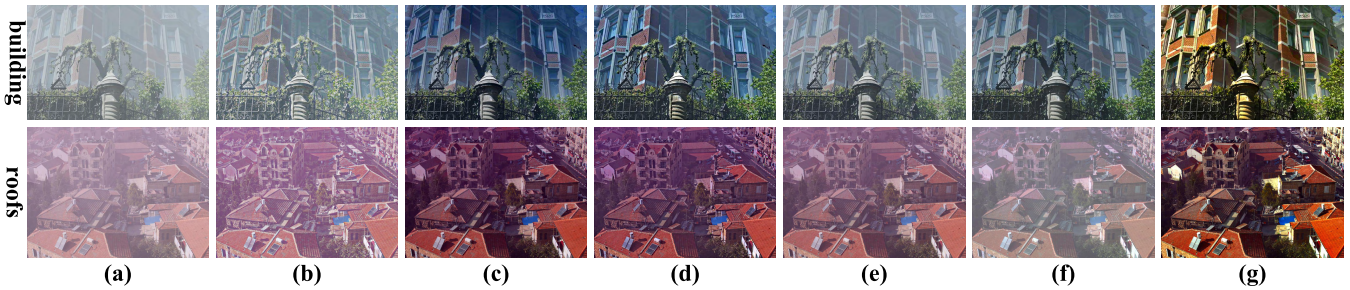

FIGURE 14. Comparison dehazing results on challenging hazy images. (a) Input hazy image. (b) Tarel *et al.*'s results. (c) He *et al.*'s results. (d) Meng *et al.*'s results. (e) Zhu *et al.*'s results. (f) Choi *et al.*'s results. (g) Our results.

near depth edges in Tarel *et al.*'s method. Similarly, there still exist halo artifacts around the leaves in He *et al.*'s and Zhu *et al.*'s methods. Although Meng *et al.*'s and Choi *et al.*'s methods can completely avoid halo artifacts, those restored haze-free images may produce color distortion and oversaturation respectively. In contrast, our achieved results are able to alleviate halo artifacts, and preserve the authenticity of the colors simultaneously. For other two hazy images "bikes" and "flag", our dehazing results are close to those obtained by He *et al.*'s method in the close view. Nevertheless, in the distant view, our dehazing results can exhibit more scene details compared with He *et al.*'s method, which is superior to other dehazing methods on human visual effects.

For the hazy images containing large sky region, Fig. 13 provides comparison dehazing results obtained by different algorithms. In Fig. 13(b) and 13(f), the dehazing results obviously suffer from over-enhancement and the sky region appears color distortion in Tarel *et al.*'s method. As can be seen in Fig. 13(c) and 13(d), the sky region tends to yield color distortion with different degrees. Despite no color distortion in Zhu *et al.*'s method, the recovered scene looks unclear and faint such as the close view in Fig. 13(e). It can be found that our approach can achieve visually compelling results in the sky region without affecting the image contrast of non-sky region, as shown in Fig. 13(g).

Finally, to prove how well six dehazing methods work on some challenging hazy images, two typical images characterized by color-shifts are selected for testing the color restoration and dehazing effect. Fig. 14 illustrates the haze-free images obtained by six different methods. From Fig. 14(b)-14(f), even though the restored images can increase the visibility of the input hazy images, the color distortions are also aggravated at the same time. Conversely, our proposed approach can restore the genuine colors of the scene and generate comparable and even more natural dehazing results, as indicated in Fig. 14(g).

B. QUANTITATIVE COMPARISON

In order to compare and assess six dehazing algorithms quantitatively, we perform two types of no-reference objective evaluation criteria based on visible edges and image color provided by Hautire *et al.* [31], Huang *et al.* [32] and Guo *et al.* [30]. Our used assessment methods mainly include five indicators: the ratio of new visible edges e, the average gradient ratio after and before restoration $\bar{r}$, color naturalness index CNI, color colorfulness index CCI and contrast-naturalness-colorfulness CNC. e and $\bar{r}$ mainly assess the ability of contrast restoration, and CNI and CCI are used for evaluating naturalness and colorfulness of color images from the perspective of color saturation. The last indicator CNC is a evaluation index to assess the algorithm performance comprehensively. Generally, the higher the values of these five indicators are, the better the dehazing approach performs.

TABLE 2. Five indicators calculated on the image in Fig. 12.

Methods	house				
	e	$\bar{r}$	CCI	CNI	CNC
Tarel *et al.* [11]	0.1914	1.8015	67.0123	0.9745	3.2687
He *et al.* [13]	0.0855	1.0760	60.1880	0.9231	3.0333
Meng *et al.* [18]	0.1427	1.7035	62.9820	0.9707	3.2199
Zhu *et al.* [20]	0.0904	1.1463	54.1819	0.8874	2.8748
Choi *et al.* [21]	0.0649	1.7020	67.1646	0.8578	2.8583
Ours	0.1175	1.2533	59.9014	0.9379	3.0853

TABLE 3. Five indicators calculated on the image in Fig. 13.

Methods	mountain				
	e	$\bar{r}$	CCI	CNI	CNC
Tarel *et al.* [11]	0.4573	1.4632	47.4579	0.7003	2.2706
He *et al.* [13]	0.1402	1.1741	42.72	0.8369	2.6326
Meng *et al.* [18]	0.1446	1.2689	49.5532	0.9190	2.95
Zhu *et al.* [20]	0.1013	1.1183	42.9585	0.7723	2.4255
Choi *et al.* [21]	0.1018	1.2411	45.5585	0.7955	2.5184
Ours	0.1127	1.5101	58.0159	0.8835	2.8930

Table 2-4 show quantitative values computed on the top row results in Fig. 12, Fig. 13 and Fig. 14. By analysing Table 2-4, Tarel *et al.*'s and Meng *et al.*'s methods can obtain large values of e, $\bar{r}$ and CNC, which is not in line with human visual perception. This is because of these objective indicators do not take spurious edges and color fidelity into account. Oversaturation of Tarel *et al.*'s results and color skew of Meng *et al.*'s results usually yield high values of e, $\bar{r}$ and CNC. In addition to these two algorithms, the dehazing

TABLE 4. Five indicators calculated on the image in Fig. 14.

Methods	building				
	e	$\bar{r}$	CCI	CNI	CNC
Tarel *et al.* [11]	0.9826	2.2929	22.4950	0.4561	1.3730
He *et al.* [13]	1.2123	2.1069	37.3105	0.9698	3.1367
Meng *et al.* [18]	1.1182	2.9050	36.5925	0.8847	2.8455
Zhu *et al.* [20]	0.5747	1.5591	20.7632	0.4390	1.2860
Choi *et al.* [21]	0.9062	1.9432	26.1652	0.6313	1.9307
Ours	1.4923	3.2856	38.6524	0.9646	3.1614

results obtained by our method can generate the highest value of *CNC* in most cases, which can demonstrate that our proposed approach can restore the haze-free images with vivid color and high scene visibility.

V. CONCLUSION

In this paper, we put forward a novel single image dehazing method via large sky region segmentation and multiscale opening dark channel model (MODCM). Under the statistical observation, a simple yet effective detection algorithm based on the thinking of classification is provided to extract the large sky region from the hazy image. On the basis of the detection result, the estimate of the atmospheric light can be obtained more accurately using two different strategies. Moreover, an improved dark channel model, called MODCM, is proposed for preserving scene structure details and preventing halo artifacts, which can adaptively choose different patch sizes to calculate the dark channel. Meanwhile, the gradient domain guided filter is adopted to refine the initial transmission map because of its accuracy near edges. Finally, qualitative and quantitative comparison of three group experiments prove that the proposed approach can remove the haze effectively and keep the authenticity of the colors better.

However, there are still some limitations in our method. Although our proposed large sky region detection method can deal with most hazy images well, our summarized features of sky region are far from enough. Therefore, we will fully dig out and take advantage of more effective and intrinsic features such as color and texture to train a superior classification model in the future work. In terms of the computation time, the proposed dehazing method still has room to improve its efficiency by processing the atmospheric light estimation and the transmission map in parallel. Besides the parallel processing and hardware acceleration, how to reduce the computation cost further should be also studied in our future research.

ACKNOWLEDGMENT

The authors would like to thank the editors and anonymous reviewers for their constructive comments.

REFERENCES

[1] J. Shi and K.-J. Yang, "An improved method of removing fog and haze effect from images," in *Proc. 4th Int. Conf. Machinery, Mater. Inf. Technol. Appl. (ICMMITA)*, Xi'an, China, Dec. 2016, pp. 1674–1679.
[2] H. Zhang and Q. Ye, "Fog-degraded image clearness based on wavelet fusion," in *Proc. Int. Conf. Intell. Syst. Design Eng. Appl. (ISDEA)*, Changsha, China, Oct. 2010, pp. 759–761.
[3] K. R. Joshi and R. S. Kamathe, "Quantification of retinex in enhancement of weather degraded images," in *Proc. Int. Conf. Audio, Lang. Image Process.*, Jul. 2008, pp. 1229–1233.
[4] Y. Y. Schechner, S. G. Narasimhan, and S. K. Nayar, "Instant dehazing of images using polarization," in *Proc. IEEE Conf. Comput. Vis. Pattern Recognit. (CVPR)*, Dec. 2001, pp. I-325–I-332.
[5] Y. Y. Schechner, S. G. Narasimhan, and S. K. Nayar, "Polarization-based vision through haze," *Appl. Opt.*, vol. 42, no. 3, pp. 511–525, Jan. 2003.
[6] S. G. Narasimhan and S. K. Nayar, "Contrast restoration of weather degraded images," *IEEE Trans. Pattern Anal. Mach. Learn.*, vol. 25, no. 6, pp. 713–724, Jun. 2003.
[7] J. Kopf *et al.*, "Deep photo: Model-based photograph enhancement and viewing," *ACM Trans. Graph.*, vol. 27, no. 5, p. 116, Dec. 2008.
[8] S. G. Narasimhan and S. K. Nayar, "Interactive (de)weathering of an image using physical models," in *Proc. IEEE Workshop Color Photometric Methods Comput. Vis.*, Nice, France, Oct. 2003, pp. 1–7.
[9] R. T. Tan, "Visibility in bad weather from a single image," in *Proc. IEEE Conf. Comput. Vis. Pattern Recognit. (CVPR)*, Anchorage, AK, USA, Jun. 2008, pp. 1–8.
[10] R. Fattal, "Single image dehazing," *ACM Trans. Graph.*, vol. 27, no. 3, p. 72, Aug. 2008.
[11] J.-P. Tarel and N. Hautiere, "Fast visibility restoration from a single color or gray level image," in *Proc. IEEE 12th Int. Conf. Comput. Vis. (ICCV)*, Kyoto, Japan, Sep. 2009, pp. 2201–2208.
[12] J.-P. Tarel, N. Hautière, A. Cord, D. Gruyer, and H. Halmaoui, "Improved visibility of road scene images under heterogeneous fog," in *Proc. IEEE Intell. Vehicles Symp. (IV)*, San Diego, CA, USA, Jun. 2010, pp. 478–485.
[13] K. He, J. Sun, and X. Tang, "Single image haze removal using dark channel prior," *IEEE Trans. Pattern Anal. Mach. Intell.*, vol. 33, no. 12, pp. 2341–2353, Dec. 2011.
[14] K. He, J. Sun, and X. Tang, "Guided image filtering," *IEEE Trans. Pattern Anal. Mach. Intell.*, vol. 35, no. 6, pp. 1397–1409, Jun. 2013.
[15] K. B. Gibson, D. T. Vo, and T. Q. Nguyen, "An investigation of dehazing effects on image and video coding," *IEEE Trans. Image Process.*, vol. 21, no. 2, pp. 662–673, Feb. 2012.
[16] K. Nishino, L. Kratz, and S. Lombardi, "Bayesian defogging," *Int. J. Comput. Vis.*, vol. 98, no. 3, pp. 263–278, Jul. 2012.
[17] G. Wang, G. Ren, L. Jiang, and T. Quan, "Single image dehazing algorithm based on sky region segmentation," *Inf. Technol. J.*, vol. 12, no. 6, pp. 1168–1175, 2013.
[18] G. Meng, Y. Wang, J. Duan, S. Xiang, and C. Pan, "Efficient image dehazing with boundary constraint and contextual regularization," in *Proc. IEEE Int. Conf. Comput. Vis. (ICCV)*, Dec. 2013, pp. 617–624.
[19] J. Li, H. Zhang, D. Yuan, and M. Sun, "Single image dehazing using the change of detail prior," *Neurocomputing*, vol. 156, pp. 1–11, May 2015.
[20] Q. Zhu, J. Mai, and L. Shao, "A fast single image haze removal algorithm using color attenuation prior," *IEEE Trans. Image Process.*, vol. 24, no. 11, pp. 3522–3533, Nov. 2015.
[21] L. K. Choi, J. You, and A. C. Bovik, "Referenceless prediction of perceptual fog density and perceptual image defogging," *IEEE Trans. Image Process.*, vol. 24, no. 11, pp. 3888–3901, Nov. 2015.
[22] B. Cai, X. Xu, K. Jia, C. Qing, and D. Tao, "DehazeNet: An end-to-end system for single image haze removal," *IEEE Trans. Image Process.*, vol. 25, no. 11, pp. 5187–5198, Nov. 2016.
[23] F. Kou, W. Chen, C. Wen, and Z. Li, "Gradient domain guided image filtering," *IEEE Trans. Image Process.*, vol. 24, no. 11, pp. 4528–4539, Nov. 2015.
[24] E. J. McCartney, *Optics of the Atmosphere: Scattering by Molecules and Particles*. New York, NY, USA: Wiley, 1976.
[25] L. Xu, C. Lu, Y. Xu, and J. Jia, "Image smoothing via L_0 gradient minimization," *ACM Trans. Graph.*, vol. 30, no. 6, p. 174, Dec. 2011.
[26] J.-H. Kim, J.-Y. Sim, and C.-S. Kim, "Single image dehazing based on contrast enhancement," in *Proc. IEEE Int. Conf. Acoust., Speech, Signal Process. (ICASSP)*, May 2011, pp. 1273–1276.
[27] J. Yu, C. Xiao, and D. Li, "Physics-based fast single image fog removal," in *Proc. IEEE 10th Int. Conf. Signal Process. (ICSP)*, Beijing, China, Oct. 2010, pp. 1048–1052.
[28] C.-C. Weng, H. Chen, and C.-S. Fuh, "A novel automatic white balance method for digital still cameras," in *Proc. IEEE Int. Symp. Circuits Syst. (ISCAS)*, Kobe, Japan, May 2005, pp. 3801–3804.

[29] F. Drago, K. Myszkowski, T. Annen, and N. Chiba, "Adaptive logarithmic mapping for displaying high contrast scenes," *Comput. Graph. Forum*, vol. 22, no. 3, pp. 419–426, Sep. 2003.
[30] F. Guo and Z. Cai, "Objective assessment method for the clearness effect of image defogging algorithm," *Acta Autom. Sin.*, vol. 38, no. 9, pp. 1410–1419, Sep. 2012.
[31] N. Hautière, J.-P. Tarel, D. Aubert, and É. Dumont, "Blind contrast enhancement assessment by gradient ratioing at visible edges," *Image Anal. Stereol. J.*, vol. 27, no. 2, pp. 87–95, Jun. 2008.
[32] K.-Q. Huang, Q. Wang, and Z.-Y. Wu, "Natural color image enhancement and evaluation algorithm based on human visual system," *Comput. Vis. Image Understand.*, vol. 103, no. 1, pp. 52–63, 2006.
[33] J. Sun, W. Xu, and B. Feng, "Adaptive parameter control for quantum-behaved particle swarm optimization on individual level," in *Proc. IEEE Int. Conf. Syst., Man Cybern.*, Oct. 2005, pp. 3049–3054.
[34] A. Levin, D. Lischinski, and Y. Weiss, "A closed-form solution to natural image matting," *IEEE Trans. Pattern Anal. Mach. Intell.*, vol. 30, no. 2, pp. 228–242, Feb. 2008.

YUN LIU (S'16) received the B.S. degree in computer science and technology from Xinyang Normal University and the M.S. degree in computer science and technology from Sichuan University, Chengdu, China, where he is currently pursuing the Ph.D. degree with the School of Computer Science. His current research interests include digital image processing, computer vision, and machine learning.

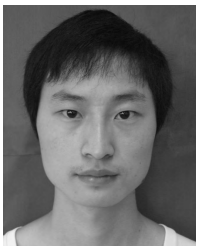

HEJIAN LI received the B.E. degree in mechatronic engineering from Xihua University in 2013. He is currently pursuing the M.S. degree with the School of Computer Science, Sichuan University, Chengdu, China. His current research interests include digital image processing and computer vision.

MINGHUI WANG received the M.S. degree from Xidian University and the Ph.D. degree from Northwestern Polytechnical University. He is currently a Professor with the College of Computer Science, Sichuan University. His current research interests are information fusion and computer vision.